Forecasting the Contribution of Polarized Extragalactic Radio Sources in CMB Observations

G. Puglisi[1,2], V. Galluzzi[3,4], L. Bonavera[5], J. Gonzalez-Nuevo[5], A. Lapi[1], M. Massardi[3,6], F. Perrotta[1], C. Baccigalupi[1,2], A. Celotti[1,2,7], and L. Danese[1]

[1] SISSA- International School for Advanced Studies, Via Bonomea 265, I-34136 Trieste, Italy; giuspugl@sissa.it
[2] INFN-National Institute for Nuclear Physics, Via Valerio 2, I-34127 Trieste, Italy
[3] INAF, Istituto di Radioastronomia, Via Piero Gobetti 101, I-40129 Bologna, Italy
[4] Dipartimento di Fisica e Astronomia, Università di Bologna, via Gobetti 93/2, I-40129 Bologna, Italy
[5] Departamento de Física, Universidad de Oviedo, C. Federico García Lorca 18, E-33007 Oviedo, Spain
[6] Italian Alma Regional Centre, Istituto di Radioastronomia, Via Piero Gobetti 101, I-40129 Bologna, Italy
[7] INAF, Osservatorio Astronomico di Brera, via Bianchi 46, I-23807 Merate (LC), Italy

Received 2017 December 26; revised 2018 February 21; accepted 2018 February 28; published 2018 May 9

Abstract

We combine the latest data sets obtained with different surveys to study the frequency dependence of polarized emission coming from extragalactic radio sources (ERS). We consider data over a very wide frequency range starting from 1.4 GHz up to 217 GHz. This range is particularly interesting since it overlaps the frequencies of the current and forthcoming cosmic microwave background (CMB) experiments. Current data suggest that at high radio frequencies ($\nu \geqslant 20$ GHz) the fractional polarization of ERS does not depend on the total flux density. Conversely, recent data sets indicate a moderate increase of polarization fraction as a function of frequency, physically motivated by the fact that Faraday depolarization is expected to be less relevant at high radio frequencies. We compute ERS number counts using updated models based on recent data, and we forecast the contribution of unresolved ERS in CMB polarization spectra. Given the expected sensitivities and the observational patch sizes of forthcoming CMB experiments, about $\sim$200 (up to $\sim$2000) polarized ERS are expected to be detected. Finally, we assess that polarized ERS can contaminate the cosmological B-mode polarization if the tensor-to-scalar ratio is <0.05 and they have to be robustly controlled to de-lens CMB B-modes at the arcminute angular scales.

Key words: cosmic background radiation – cosmology: observations – polarization – quasars: general – radio continuum: galaxies

1. Introduction

The cosmic microwave background (CMB) is a relic radiation generated at the decoupling of matter and radiation as the temperature of the universe dropped below 3000 K. Its temperature and polarization anisotropies can be exploited to probe the early stages of the universe when an exponential expansion, the so-called *inflation*, might have occurred (Guth 1981; Starobinsky 1982).

In recent decades, several experiments have tried to measure the CMB polarized signal in order to find the imprints on its polarized anisotropies of a stochastic background of primordial gravitational waves (PGW) that might have been produced during the inflationary phase. Polarization anisotropies are commonly decomposed into two scalar quantities called E- and B-modes (Hu & White 1997; Seljak & Zaldarriaga 1997) and, to date, many efforts have been made to observe the latter since their amplitude at the degree scale is expected to come mainly from PGW.

On one hand, E-mode photons get deflected via gravitational interaction by intervening matter of large-scale structures on the path toward us, producing the so-called lensing B-modes on an arcminute scale. Lensing B-modes have been observed since 2014 (The Polarbear Collaboration et al. 2014, 2017; Keisler et al. 2015; Louis et al. 2017) with better and better accuracy and they represent a powerful tool to probe the large-scale structure of our universe. On the contrary, the primordial B-mode amplitude is unknown and is quantified by the tensor-to-scalar ratio, r, that relates the amplitude of tensor perturbations of the spacetime metric, e.g., PGW, with respect to the scalar perturbations. The joint collaboration of BICEP2 and *Planck* yielded the most recent upper limit on $r < 0.07$ at the 95% confidence level (BICEP2/Keck & Planck Collaborations et al. 2015), meaning that the primordial B-mode amplitude could be even lower than the lensing amplitude.

To date, several challenges have prevented the detection of primordial B-modes mostly because of the diffuse polarized radiation coming from the Milky Way, known as Galactic foregrounds. The list of Galactic foregrounds is long and includes anything emitting at submillimeter wavelengths between us and the CMB: thermal dust, synchrotron radiation, free–free emission, and several molecular line emissions (Planck Collaboration et al. 2016b). All these emissions are partially polarized and the main contribution comes from synchrotron and dust (both polarized up to 20% level Planck Collaboration et al. 2016c, 2016e). At high frequencies ($\nu > 90$ GHz), such a large polarization degree is produced by thermal dust grains aligning along the Galactic magnetic field lines. At low frequencies ($\nu \lesssim 70$ GHz), cosmic electrons spiralling into the Galactic magnetic field produce synchrotron radiation. Molecular lines are expected to be polarized at lower levels $\lesssim 1\%$ (Goldreich & Kylafis 1981; Puglisi et al. 2017), whereas free–free emission can essentially be considered unpolarized. This is the justification of the recent efforts aimed at observing the CMB polarization in a very wide range of frequencies and at accurately characterizing both the spatial and

frequency distribution of each Galactic polarized foreground. Moreover, such an investigation allows us to design algorithms known as component separation or foreground cleaning techniques to extract B-modes out of a multi-frequency experimental setup.

For these reasons, (i) more focal plane pixels in multiple telescopes are needed to increase sensitivity and (ii) multiband polarization measurements are required to recover the cosmic signal from the Galactic one via component separation. As the focal plane will encode a larger and larger number of detectors, the next stages in CMB experiment sensitivity will be achieved by more accurately measuring r. To date, several ground-based experiments are updating their focal planes to a step forward from the so-called CMB-Stage 2 (CMB-S2) to Stage 3 (CMB-S3, Arnold et al. 2014; Benson et al. 2014; Henderson et al. 2016), including up to 10,000 detectors observing up to 7% of the sky. The ultimate step for a B-mode detection from the ground is represented by CMB-Stage 4 experiments (CMB-S4, Abazajian et al. 2016), which will account for up to 100,000 detectors, observing half of the sky. CMB-S4 aims at measuring r with the target accuracy $\sigma(r) \sim 0.0005$.

At smaller scales, the extragalactic radio sources (ERS) and star-forming dusty galaxies are the major contaminants (Tucci et al. 2011), although the latter can also largely contribute to large angular scales due to clustering (De Zotti et al. 2015). In this work, we mostly focus on the polarized emission of ERS. To date, a few studies have been conducted regarding polarization of ERS at the frequencies of CMB experiments (see Galluzzi & Massardi 2016 or Bonavera et al. 2017a) since polarization observations in the millimeter wavelength bands are more challenging than in the centimeter bands (at $1.4 \div 20$ GHz) and extrapolations are very common in this field of research (Tucci & Toffolatti 2012).

The mechanism behind the polarized emission of radio sources is mostly due to synchrotron radiation sourced by an active galactic nucleus (AGN), where a central super-massive black hole ($10^6 \div 10^9 M_\odot$) is hosted. Most of the energy of an AGN comes from the gravitational potential energy of the material located in a thin surrounding accretion disk, released as the matter falls into the central black hole. Another component is constituted by jets (usually paired) of material ejected toward the polar directions from the black hole. Jets are observed to be very collimated and can travel very large distances. Therefore, radio galaxies sometimes present double structures, referred to as lobes, constantly fed by the jets of new energetic particles and magnetic energy.

Depending on which components dominate the emission, such complex objects can appear with different morphologies and therefore be grouped in different observational categories. One of the most important distinctions is related to the different orientations in which an AGN can be observed with respect to the line of sight (see De Zotti et al. 2010 for a wide review). If edge-on, the torus obscures the core and the inner disk, so that the emission is dominated by the optically thin radio lobes presenting a steep spectral index α at low frequencies $1 \div 5$ GHz.[8] Objects with $\alpha > 0.5$ are commonly referred as steep-spectrum radio quasars (SSRQs) and, generally, their optical counterpart is an elliptical galaxy. If seen pole-on, the brightness is dominated by the approaching jet, the emission

looks compact, and it is mostly Doppler boosted since particles move at relativistic speeds. The emission is optically thick and does not contain many optical features in the continuum but is characterized by a flat spectrum ($\alpha < 0.5$). Similar sources are called flat-spectrum radio quasars (FSRQs).

However, each source presents both of the components, i.e., a flat-spectrum core and extended steep-spectrum lobes, and it can be understood that a simple-power law cannot be applied to resemble the large radio frequency range (Massardi et al. 2011; Bonaldi et al. 2013). External and self-absorption, from free–free and synchrotron, may affect and change the dependence of S_ν, so that the spectrum could increase as a function of frequency (Galluzzi et al. 2017).

There is an increasing interest in polarization of ERS at high-radio frequencies, not only to better understand the physics behind the emitting system, e.g., the degree of ordering of the magnetic field and the direction of its field lines (Tucci et al. 2011), but also because polarized ERS will be largely detected by forthcoming CMB experiments. Furthermore, the ERS contaminating signal in the polarization power spectra cannot be neglected to assess the power spectrum of lensing B-modes. This is the reason why recent work can be found addressing this issue in the literature: De Zotti et al. (2015, 2016) predicted the contribution in polarization both for ERS and dusty galaxies at frequency channels of the Cosmic ORigin Explorer (CORE) satellite; Curto et al. (2013) estimated for future CMB missions the contamination produced by radio and far-infrared sources at the level of bispectrum considering different shapes of the primordial non-Gaussianity parameter, f_{nl}.

In Section 2, we describe the data sets we combine in order to determine the polarization dependence as a function of frequency, discussed in Section 4. In Section 3, we present the models for number counts adopted in this analysis. In Section 5, we show the results of a forecast package we developed to assess the contamination of polarized ERS in terms of CMB power spectra given the nominal specifics of current and forthcoming CMB experiments. Finally, in Section 6, we discuss and summarize our results.

2. Data

In this section, we present the data collected from publicly available catalogs. The data, summarized in Table 1, have been used to characterize the polarization fraction of ERS in about two orders of magnitude in the frequency range (i.e., from 1.4 to 217 GHz).

2.1. The S-PASS/NVSS Joint Catalog

The S-band Polarization All-Sky Survey (S-PASS) survey observed the southern sky with declination $\delta < -1°$ at 2.3 GHz with full width at half maximum (FWHM) of 8.9 arcmin both in total intensity and polarization using the 64 m Parkes Radio Telescope. Lamee et al. (2016) cross-matched it with the NRAO/VLA Sky Survey, (NVSS, Condon et al. 1998), at 1.4 GHz (45 arcsec (FWHM) and rms total brightness fluctuations of $\sim$0.29 mJy beam^{-1}). Lamee et al. (2016) aimed at generating a novel and independent polarization catalog[9] enclosing 533 bright ERS at 2.3 GHz with polarized flux density stronger than 420 mJy.

---

[8] The radio-source flux is described by a power law $S_\nu \propto \nu^{-\alpha}$ and the threshold between flat and steep spectral behavior is commonly fixed at $\alpha = 0.5$.

[9] http://vizier.cfa.harvard.edu/viz-bin/VizieR?-source=J/ApJ/829/5

Table 1
Summary of the Catalogs Used in Section 5

	Frequency [GHz]	Sky Region	FWHM	Detect. flux	90% Compl.	# Sources
NVSS	1.4	$\delta > -40°$	45″	0.29 mJy/beam	2.3 mJy	1.8×10^6
S-PASS	2.3	$\delta < -1°$	8′.9	1 mJy/beam	420 mJy	533
JVAS	8.4	$\delta \geqslant 0°, |b| \geqslant 2°.5$	0″.2	50 mJy	200 mJy	2720
CLASS	8.4	$0 \geqslant \delta \geqslant 70°$	0″.2	20 mJy	30 mJy	16503
AT20G	4.8, 8.6, 20	$\delta < 0°, |b| < 1°.5$	10″,6″, 11″	40 mJy	100 mJy/beam	5890
VLA	4.8, 8.5,	$\delta > -15°$	12″, 6″	0.7, 0.3	40 mJy	159
	22.5, 43.5		4″, 2″	0.9, 1.2 mJy/beam		
PACO	20	Ecl. lat. $<-65°$	11″	40 mJy	200 mJy	104
XPOL-IRAM	86	$\delta > 30°$	28″	0.5 Jy	1 Jy	145
PCCS2	30, 44,		32′.4, 27′.1	117, 229	427, 692	1560, 934
	70, 100,	Full sky	13′.3, 9′.7	225, 106	501, 269	1296, 1742
	143, 217		7′.3, 5′.0	75, 81 mJy	177, 152 mJy	2160, 2135

2.2. The JVAS/CLASS 8.4 GHz Catalog

We used the data from the JVAS/CLASS 8.4 GHz catalog Jackson et al. (2007),[10] which combined data taken from the Jodrell-VLA Astrometric Survey (JVAS) and the Cosmic Lens All-Sky Survey (CLASS) both observing at 8.4 GHz. The former detected 2720 sources stronger than 200 mJy in total intensity at 5 GHz and $\delta \geqslant 0°$, masking the Galactic midplane at Galactic latitude $|b| \geqslant 2°.5$. To complement JVAS, CLASS consisted of all sources with a fainter 5 GHz flux, i.e., $S > 30$ mJy observed in a sky region between $0° \leqslant \delta \leqslant 70°$. Combining the two surveys, a sample of 16,503 FSRQ intensity fluxes has been collected.

Jackson et al. (2010) were able to assess polarized fluxes for only a few objects from the 133 sources observed by the Wilkinson Microwave Anisotropy Probe (*WMAP*) at 22 and 43 GHz ($S > 1$ Jy Wright et al. 2009) with counterparts in the JVAS/CLASS catalogs. For the purposes of our work this sample was not large enough to be included in the following analysis.

However, we exploit the data selection described by Pelgrims & Hutsemékers (2015) that considered all the sources with polarized flux $\geqslant 1$ mJy in order to obtain an unbiased sample of 3858 NED identified sources. We selected 2829 sources classified by Pelgrims & Hutsemékers (2015) as QSOs and radio sources. For a complete description of the catalog and the surveys, refer to Jackson et al. (2007).

2.3. The AT20G Survey

The Australia Telescope 20 GHz (AT20G) Survey blindly observed the southern sky ($\delta < 0°$ excluding the Galactic plane strip at $|b| < 1°.5$) at 20 GHz with the Australia Telescope Compact Array (ATCA) from 2004 to 2009, (Murphy et al. 2010). The detected sources were followed up almost simultaneously at 4.8 and 8.6 GHz. The AT20G source catalog[11] includes 5890 sources at 20 GHz above the total intensity detection limit of 40 mJy, of which 3332 were detected at all the observing frequencies. Averaged over the entire area of the survey, the catalog is 91% complete above 100 mJy beam^{-1} (Murphy et al. 2010). Polarization of sources was considered detected if the following criteria were satisfied:

polarized flux density $P > 6$ mJy or at least three times larger than its rms error, and polarized fraction above 1%. Massardi et al. (2011) presented an analysis to characterize the radio spectral properties of the whole sample in both total intensity and polarization, involving 768 sources detected at 20 GHz (467 of them were also detected in polarization at 4.8 and/or at 8.6 GHz). Given the goal of this work, we include polarized flux densities from 3332 sources, 2444 of them presenting a flat spectrum in total intensity ($|\alpha_5^8| < 0.5$) and the remaining 888 a steep-spectrum source ($|\alpha_5^8| > 0.5$).

2.4. The VLA Observations

Sajina et al. (2011) presented measurements[12] in flux densities and polarization of 159 ERSs detected with the Very Large Array (VLA) at four frequency channels: 4.86, 8.46, 22.46, and 43.34 GHz. This sample was selected from the AT20G sample (Murphy et al. 2010; Massardi et al. 2011) by requiring a flux density $S > 40$ mJy in the equatorial field of the Atacama Cosmology Telescope (ACT) survey on a region at a declination north of $-15°$ and excluding the Galactic plane. The aim of this program was first to characterize the spectra and variability both in total intensity and polarization of high-frequency-selected radio sources and to improve the estimation of the ERS contamination at high frequency for CMB experiments.

In 40% of the whole sample, they detected polarized flux density in all the bands and observed an increasing trend of the polarization fraction as a function of frequency, which was more evident for SSRQs.

2.5. PACO with ATCA and ALMA

The Planck-ATCA Coeval Observations (PACO) project detected 464 sources selected from the AT20G catalog during 65 epochs between 2009 July and 2010 August, at frequencies ranging from 5.5 to 39 GHz with the ATCA. The sources were simultaneously observed (within 10 days) by the Planck satellite (Bonavera et al. 2011; Massardi et al. 2011). The project aimed at characterizing, together with Planck data, the variability and spectral behavior of sources over a wide frequency range (up to 857 GHz for some sources), in total intensity only. The catalog includes a complete sample of 159 sources selected to be brighter than 200 mJy at $\delta < 30°$ (excluding the Galactic midplane $|b| < 5°$). A sub sample of

---

[10] http://vizier.cfa.harvard.edu/viz-bin/VizieR?-source=J/MNRAS/376/371
[11] http://vizier.cfa.harvard.edu/viz-bin/VizieR?-source=J/MNRAS/402/2403

[12] http://vizier.u-strasbg.fr/viz-bin/VizieR?-source=J/ApJ/732/45

104 of these sources with ecliptic latitude $< -65°$ (which coincides with one of the deep patches most frequently scanned by the *Planck* satellite scanning strategy) has been reobserved with high sensitivity in polarization with ATCA in 2014 and 2016 in the 1.1–39 GHz frequency range (Galluzzi et al. 2017). Thirty-two of the sub samples have also been followed up at 95 GHz onto three circular regions (10° of diameter) at ecliptic latitude $< -75°$ with the Atacama Large Millimeter Array (ALMA) to better characterize the polarization properties of ERS at the frequencies of many CMB experiments and allowing an accurate study of a few reference targets that could be exploited for calibration and validation of cosmological results. Further details will be described in a companion paper (V. Galluzzi et al. 2018, in preparation). Data from both 20 and 95 GHz have been included in this analysis.

2.6. First 3.5 mm Polarimetric Survey

Agudo et al. (2010) presented, for the first time, polarimetric data at 86 GHz of a sample of 145 flat spectrum radio galaxies at different epochs (from 2005 July to 2009 October).[13] The measurements have been performed by means of the XPOL polarimeter of the IRAM 30 m telescope, by selecting the sources observed from 1978 to 1994 at $\delta > 30°$ whose total intensity was above $\gtrsim 1$ Jy. They detected above the $>3\sigma$ level 1.5% linear and 0.3% circular polarization degree for 76% and 6% of the whole sample, respectively. Remarkably, they found a factor of ~ 2 excess in the polarization fraction at 86 GHz with respect to that measured at 15 GHz.

2.7. The Second Planck Catalog of Compact Sources

We exploit data from the latest Planck Catalog of Compact Sources (PCCS2, Planck Collaboration 2015),[14] including polarimetric detection of sources between 30 and 353 GHz from 2009 August to 2013 August. The total intensity 90% completeness ranges from 177 to 692 mJy in this regime of frequencies, allowing detection of thousands of sources matched both internally (between neighbor *Planck* channels) and with external catalogs. On the contrary, the instrumental noise in polarization and the presence of polarized Galactic foregrounds limited the number of polarized sources to a few tens (with the exception of the 30 GHz channel where 113 polarized sources were detected).

It is straightforward to state that only sources with high fractional polarization have been detected by *Planck* and thus the statistics of ERS polarization can be biased upward. Bonavera et al. (2017a) recently proposed a methodology to cope with this issue by means of applying a stacking technique to *Planck* data. They used as a main sample the 30 GHz catalog, consisting of 1560 sources above $S > 427$ mJy at the 90% completeness level, and then followed the sample at higher *Planck* frequency maps. They further distinguished sources inside and outside the Galactic plane defined by the Planck Galactic mask GAL060 ($f_{sky} \approx 60\%$) and the exclusion of the Small and Large Magellanic clouds. This technique has already been applied by Stil et al. (2014) to the NVSS data set to study the faint polarized signal of ERS detected in total intensity: the signal from many weak sources is co-added to

achieve a statistical detection. Bonavera et al. (2017a) found that the ERS polarization fraction is approximately constant with frequency over the *Planck* frequency range. An alternative approach that attempts to overcome some of the intrinsic statistical limitations of the stacking technique has been recently exploited by Trombetti et al. (2017) and has obtained results comparable both with Bonavera et al. (2017a, 2017b) and with other ground-based observations.

We used both data coming from the PCCS2 catalog and from Bonavera et al. (2017a).

3. Model for Number Counts

We adopted the evolutionary model proposed by de Zotti et al. (2005, hereafter, D05) that describes the population properties of ERSs and dusty galaxies above $\nu \gtrsim 5$ GHz. The model assumes a simple analytic luminosity evolution in order to fit the available data on local luminosity functions (LF), source counts,[15] and redshift distributions for sources down to a few millijansky. It determines the epoch-dependent LF starting from local LFs for several source populations. For each population, the model adopts different evolution laws estimating a set of free parameters from available data. Recently, Bonato et al. (2017) and Mancuso et al. (2017) improved the predictions of the D05 model by updating the LF and redshift evolution with state-of-the-art data of radio-emitting star-forming galaxies and AGNs.

The D05 model assumes a power law spectrum for each considered population of ERS and each one is described by one (or at most two) constant spectral index. These simple assumptions do not hold when large frequency ranges are taken into account. Departures from single power-law spectra are expected because of (i) electron ageing, (ii) transition from an optically thick to an optically thin regime, and (iii) different components yielding different spectral contributions at different frequencies. Therefore, this simplified model requires adjustment when source count measurements are observed at frequencies >40 GHz.

Tucci et al. (2011) showed that radio spectra in AGN cores can differ from a single power law when large frequency intervals are considered. In particular, they focused on the blazar spectra for which a steepening of the spectral index from 0.5 to 1.2 has been observed (Planck Collaboration et al. 2011a, 2011b) due to the transition from optically thick to optically thin synchrotron emission of AGN jets (Kellermann 1966; Blandford & Koenigl 1979). Therefore, Tucci et al. (2011) proposed the so-called *C2Ex* model that assumes a spectral break and different parameters for BL Lacs and FSRQs and allows us to properly fit the number counts especially at high-frequency ($\nu \geqslant 100$ GHz). Furthermore, Planck Collaboration (2015, XXVI) found that all radio sources observed at the Low Frequency Instrument (LFI) channels present flat and narrow spectral index distribution with $\alpha_{LFI} \lesssim 0.2$, whereas sources in the High Frequency Instrument (HFI) catalogs have a broader distribution showing a steeper spectral index, $\alpha_{HFI} \gtrsim 0.5$ and these findings supports the scenario of BL Lac transition happening at larger frequencies $\nu > 100$ GHz with respect to the FSRQ one (at $10 < \nu < 100$ GHz).

In Figure 1, we plot the differential number counts, $n(S)$, predicted with D05 and C2Ex models as blue and gray thick solid lines, respectively. The top (bottom) panel refers to
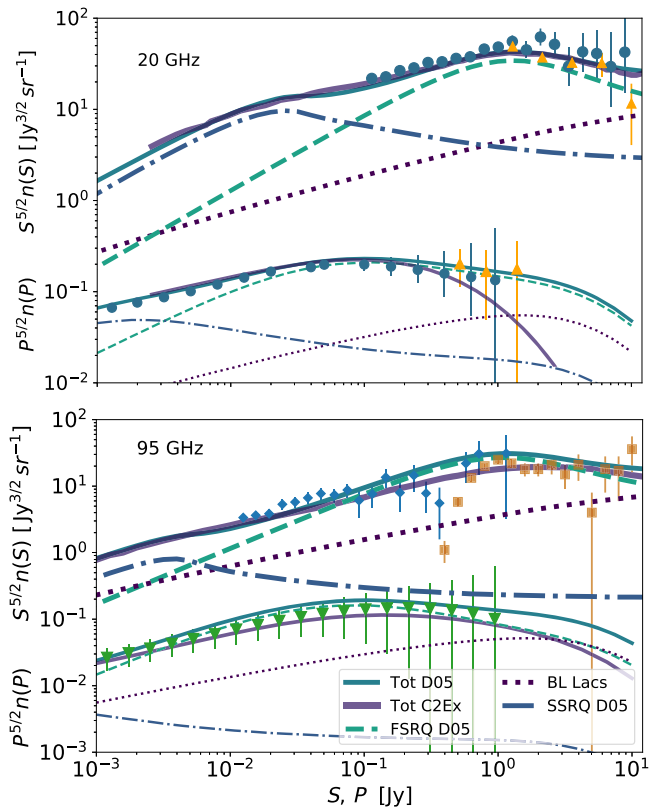
Figure 1. Euclidean differential number counts at (top) 20 and (bottom) 95 GHz. Thick dotted, dashed, dotted–dashed, and solid lines are, respectively, the number counts of BL Lacs, FSRQs, SSRQs, and their total contribution predicted by the D05 model (de Zotti et al. 2005). The thick solid gray line shows the number counts prediction from the C2Ex model (Tucci et al. 2011). Thinner lines follow the same color scheme as the thick ones and refer to polarization number counts, computed via a convolution with a log-normal distribution function fitted from the data. Number count estimates from several surveys are also shown. (Top) The circle data points in the upper curves are data from AT20G (Massardi et al. 2008), whereas upper triangles are from WMAP5-yr survey (K-band, Massardi et al. 2009); in lower curves polarization number counts from a resampling of PACO data (Galluzzi et al. 2018, circles) and from *WMAP* polarization point source catalog (Lopez-Caniego et al. 2009, upper triangles). (Bottom) Diamonds in upper curves are number counts from SPT (Mocanu et al. 2013), squares are from *Planck* ERCSC catalog (Planck Collaboration et al. 2011b); the lower triangles have been obtained from a bootstrap resampling of 32 polarized fluxes detected with PACO at 95 GHz.

number counts at 20 (95) GHz.[16] We also plot the contributions estimated by the D05 model for BL Lacs, FSRQs, and SSRQs, respectively, as dotted, dashed, and dotted–dashed lines. To compare the quantities with those expected in a Euclidean universe, counts are normalized by a factor of $S^{5/2}$. The data points shown are number counts as measured by the AT20G survey (Massardi et al. 2008, blue circles), from the South Pole Telescope (SPT, Vieira et al. 2010; Mocanu et al. 2013, blue diamonds), from *WMAP* (Massardi et al. 2009, yellow upper triangles), and from *Planck* (Planck Collaboration et al. 2011b, 2013, yellow squares).

The lower thinner curves in Figure 1 are Euclidean normalized differential polarized emission number counts, $P^{5/2} n(P)$, computed from polarized flux density measurements and will be discussed in Section 4.

---

[16] Source number counts for a wider range of frequencies are shown in Figure 6.

By comparing the predictions from the two models, we find that both are in reasonable agreement, with differences well below the uncertainties at 20 GHz. However, as discussed above and shown in the bottom panel of Figure 1, number counts estimated with D05 are systematically a factor of ∼2 higher than the C2Ex counts at larger fluxes of 100 mJy, consistent with the findings of Planck Collaboration et al. (2011b).

In the following, we make use of both D05 and C2Ex models to assess, respectively, conservative and realistic estimates of polarized ERS to CMB measurements.

4. Statistical Properties of the ERS Polarization Fraction

Polarization number counts have to be assessed to know how many sources can be detected at a certain polarized flux density, $P = \sqrt{Q^2 + U^2}$, with Q and U being the linear polarization Stokes parameters. Polarization measurements at millimeter wavelengths are scarce because of the faintness of the polarized signal, so that both high sensitivity and robust estimates of systematic effects are required. Furthermore, completeness is very hard to achieve with polarized samples. This is the reason why, to date, extrapolations from low frequency observations ($1.4 \div 5$ GHz) are commonly adopted although the uncertainties due to intra-beam effects and bandwidth depolarization may seriously affect the estimation.

To address this issue, several works in the literature (Battye et al. 2011; Tucci & Toffolatti 2012; Massardi et al. 2013; Bonavera et al. 2017a) have considered the probability function $\mathcal{P}(\Pi)$ of the polarization fraction, $\Pi = P/S$. Differential polarization number counts can be defined as

$$
n(P) = N \int_{S_0 = P}^{\infty} \mathcal{P}(P, S) \, dS = N \int_{S_0 = P}^{\infty} \mathcal{P}(\Pi, S) \frac{dS}{S}
$$
$$
= \int_{S_0 = P}^{\infty} \mathcal{P}(\Pi) n(S) \frac{dS}{S}, \tag{1}
$$

where N is the total number of sources with $S \geqslant S_0$, $\mathcal{P}(P, S)$ and $\mathcal{P}(\Pi, S)$ are the probability functions of finding a source with flux S and polarized flux P or polarization fraction Π and both can be constrained from observations.

Notice that, in the last equation of (1), we assume that Π and S are statistically independent. On one hand, recent results at low frequencies indicate that this might not be the case: Stil et al. (2014) found that fainter sources (∼1 mJy) of the NVSS catalog present a higher median fractional polarization. These results were confirmed by Lamee et al. (2016) with S-PASS: they found indications of a possible correlation between the polarization fraction and total intensity of steep-spectrum sources ranging from 0.42 to 10 Jy, whereas the correlation disappears when FSRQs are involved. On the other hand, at higher frequencies (above 20 GHz), Massardi et al. (2008) and Tucci & Toffolatti (2012) did not find a clear correlation between Π and S (at fluxes above 500 mJy) for both FSRQs and SSRQs, but they found fractional polarization correlating at frequencies between 4.8 and 20 GHz.

To date, surveys at high frequencies have not been sensitive enough to probe fainter polarized fluxes in order to seek whether this assumption holds or not. Tucci et al. (2004) further argued that at higher frequencies we observe two possible effects: (i) depolarization from Faraday rotation is essentially negligible at frequencies above $\nu \gtrsim 10$ GHz, (ii) by observing compact objects (i.e., FSRQs) at increasingly higher
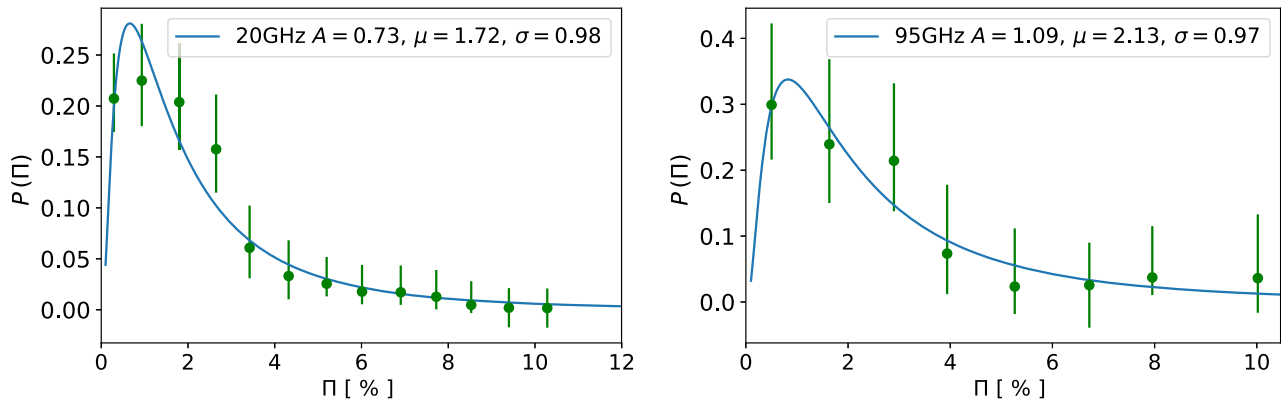
Figure 2. The distribution function of polarization fraction for data at 20 GHz (left) and at 95 GHz (right). The best-fit values of log-normal parameters are shown. The reduced $\tilde{\chi}^2$ estimated from the fit is 0.13 and 0.15, respectively, for left and right panels.

frequencies, we probe regions that are progressively closer to the nucleus, where the magnetic field is expected to be highly ordered. Consequently if this is the case, the polarization fraction may increase with frequency.

Given the goals of our work and the fact that frequencies above 10 GHz are involved in the forecast analysis, we assume polarized fraction and flux density are uncorrelated and statistically independent, but we look for some eventual dependence of Π as a function of frequency.

Following Battye et al. (2011), we model $\mathcal{P}(\Pi)$ by means of a log-normal distribution, i.e.,

$$\mathcal{P}(\Pi) = \frac{A}{\sqrt{2\pi\sigma^2}\,\Pi} \exp\left[-\frac{(\ln(\Pi/\mu))^2}{2\sigma^2} \right], \qquad (2)$$

where μ and σ are, respectively, the median and the standard deviation in log. Notice that Equation (2) holds only if $0 \leqslant \Pi < \infty$. Although an infinite value of Π does not have any physical meaning (synchrotron emission can be polarized up to 75%), the values of μ and σ are orders of magnitude smaller. Thus Π can be effectively assumed to range up to a large value. This allows us to write a good approximation of the fractional polarization by a combination of the log-normal parameters[17]

$$\langle\Pi\rangle \approx \mu e^{\frac{1}{2}\sigma^2}, \qquad (3)$$

$$\langle\Pi^2\rangle \approx \mu^2 e^{2\sigma^2}, \qquad (4)$$

$$\Pi_{\mathrm{med}} \approx \mu. \qquad (5)$$

We derive the polarization fraction distribution by using a bootstrap-resampling method outlined in Austermann et al. (2009). This generates N_{resamp} simulations of the catalog and values for unpolarized and polarized flux densities are randomly assigned for each source, from a normal distribution $\mathcal{N}(\mu_{\mathrm{src}}, \sigma_{\mathrm{src}})$ peaking at the observed value μ_{src} and with a width σ_{src} equal to the flux uncertainty. In the case of upper limits, a random number is extracted from a normal distribution centered on 0 and with width σ_{src}. For each resampling, we compute the polarization fraction and the values are distributed across bins (ranging from 5 to 15 bins depending on the number of data collected in each catalog). The final distribution is thus given by the mean value within each bin and vertical error bars computed by means of Poisson statistics, at 68% of

confidence level (CL, Gehrels 1986), counting the observed sources in each polarization fraction bin. Finally, a log-normal distribution function (2) is fitted from each data set and $\langle\Pi\rangle$, $\langle\Pi^2\rangle$, and Π_{med} are then estimated from the log-normal parameters μ and σ as in (3)–(5). In Figure 2 we show the polarization fraction distributions from PACO-ATCA at 20 GHz and PACO-ALMA at 95 GHz (the best-fit parameters of the other data sets used in this analysis are summarized in Table 2). In the top panel of Figure 1 we show the polarization number counts computed by Galluzzi et al. (2018) at 20 GHz (blue circles) as a result of the convolution of total intensity number counts with the log-normal distribution $\mathcal{P}(\Pi)$ as in Equation (1). We further overlap the predicted total counts from both the D05 (solid thin blue) and C2Ex (solid thin gray) models convolved with the distribution function. As already stated in Section 3, at 20 GHz, both models are equivalent even for polarized number counts.

In the bottom panel of Figure 1, the polarized number counts at 95 GHz coming from the PACO-ALMA sample of 32 sources are shown as lower green triangles. Given the paucity of this sample, we resample it by means of 1000 bootstrap resamplings. The resampled source counts (shown as green triangles in Figure 1) are then computed in a similar manner as for the 20 GHz observations and are summarized in the companion paper by V. Galluzzi et al. (2018, in preparation). The error bar estimation of each data point includes the Poissonian 68% CL uncertainties (Gehrels 1986) plus the error derived from the uncertainties of log-normal parameters δ_A, δ_μ, and δ_σ (summarized in Table 2). This error has been assessed by means of differencing the number counts convolved with an upper and a lower log-normal function, respectively estimated at maximum and minimum values of log-normal parameters.

We would like to stress that this is the first time that number counts from the PACO-ALMA sample have been computed and exploited for this kind of analysis. Notice that the data are very well fitted by both predictions.

The estimated values of $\langle\Pi\rangle$, Π_{med}, and $\langle\Pi^2\rangle^{1/2}$ for FSRQ (left panel) and SSRQ (right panel) are shown in Figure 3. By comparing the two panels, we note that the SSRQ fractional polarizations increase with frequency. Although this could be simply related to observational bias (at higher frequencies, steep-spectrum sources contributes at fainter fluxes), such frequency dependence of Π for SSRQs has been already discussed in Tucci & Toffolatti (2012). On the contrary, the fractional polarization measured for the FSRQ remains almost

---

[17] For further details refer to Battye et al. (2011).

Table 2
Values of Log-normal Parameters Obtained by Fitting Data from Each Catalog

ν[GHz]	N_{src}	A	μ	σ	$\langle\Pi\rangle$	Π_{med}	$\langle\Pi^2\rangle^{1/2}$	Reference
				Flat-spectrum Sources				
1.4	82	0.54 ± 0.08	1.73 ± 0.24	1.05 ± 0.09	2.98 ± 0.64	1.72 ± 0.24	5.15 ± 1.53	Lamee et al. (2016)
2.3	82	0.53 ± 0.07	1.51 ± 0.13	1.05 ± 0.07	2.64 ± 0.36	1.52 ± 0.13	4.59 ± 0.87	Lamee et al. (2016)
4.8	2335	1.57 ± 0.07	2.36 ± 0.02	0.75 ± 0.01	3.14 ± 0.03	2.37 ± 0.02	4.16 ± 0.08	Murphy et al. (2010)
8.6	2335	1.55 ± 0.02	2.46 ± 0.01	0.73 ± 0.01	3.21 ± 0.03	2.46 ± 0.01	4.20 ± 0.06	Murphy et al. (2010)
8.6	2827	0.52 ± 0.01	2.41 ± 0.05	0.76 ± 0.01	3.23 ± 0.08	2.41 ± 0.05	4.31 ± 0.14	Pelgrims & Hutsemékers (2015)
4.8	109	0.60 ± 0.06	2.02 ± 0.13	0.84 ± 0.05	2.89 ± 0.28	2.02 ± 0.13	4.12 ± 0.55	Sajina et al. (2011)
8.6	109	0.74 ± 0.14	2.12 ± 0.24	0.84 ± 0.09	3.01 ± 0.51	2.12 ± 0.23	4.27 ± 1.02	Sajina et al. (2011)
22	155	1.36 ± 0.09	3.1 ± 0.10	0.88 ± 0.03	4.57 ± 0.22	3.10 ± 0.09	6.74 ± 0.46	Sajina et al. (2011)
43	111	2.59 ± 0.08	4.48 ± 0.06	1.00 ± 0.03	7.42 ± 0.17	4.47 ± 0.06	12.32 ± 0.41	Sajina et al. (2011)
20	104	0.73 ± 0.05	1.73 ± 0.16	0.98 ± 0.06	2.91 ± 0.42	1.73 ± 0.16	4.89 ± 0.99	Galluzzi et al. (2018)
89	145	1.20 ± 0.05	2.86 ± 0.10	0.64 ± 0.03	3.52 ± 0.17	2.86 ± 0.10	4.32 ± 0.28	Agudo et al. (2010)
95	32	1.09 ± 0.21	2.13 ± 0.23	0.97 ± 0.09	3.20 ± 0.60	2.07 ± 0.24	4.94 ± 1.32	This work
30	114	1.51 ± 0.23	2.05 ± 0.36	1.08 ± 0.08	3.69 ± 0.92	2.06 ± 0.37	6.61 ± 2.19	Planck Collaboration (2015)
44	30	2.63 ± 0.26	2.72 ± 0.26	0.77 ± 0.11	3.69 ± 0.66	2.73 ± 0.26	5.00 ± 1.32	Planck Collaboration (2015)
70	34	3.91 ± 0.55	2.52 ± 0.05	0.58 ± 0.06	2.97 ± 0.15	2.51 ± 0.05	3.52 ± 0.30	Planck Collaboration (2015)
100	20	2.18 ± 0.28	5.15 ± 0.69	0.80 ± 0.10	7.19 ± 1.59	5.17 ± 0.73	9.99 ± 3.07	Planck Collaboration (2015)
143	25	3.13 ± 0.10	5.98 ± 0.16	0.80 ± 0.04	8.39 ± 0.35	6.02 ± 0.13	11.69 ± 0.80	Planck Collaboration (2015)
217	11	3.44 ± 0.32	3.74 ± 0.29	0.88 ± 0.11	5.47 ± 0.34	3.70 ± 0.27	8.09 ± 1.09	Planck Collaboration (2015)
				Steep-spectrum Sources				
1.4	388	1.12 ± 0.08	1.47 ± 0.11	1.05 ± 0.08	2.56 ± 0.35	1.47 ± 0.11	4.45 ± 0.95	Lamee et al. (2016)
2.3	388	1.78 ± 0.07	1.93 ± 0.06	0.80 ± 0.05	2.66 ± 0.14	1.93 ± 0.06	3.66 ± 0.31	Lamee et al. (2016)
4.8	952	2.07 ± 0.07	2.83 ± 0.07	0.81 ± 0.04	3.92 ± 0.15	2.84 ± 0.08	5.43 ± 0.37	Murphy et al. (2010)
8.4	952	3.02 ± 0.03	2.13 ± 0.12	1.13 ± 0.03	4.85 ± 0.05	3.02 ± 0.05	7.79 ± 0.18	Murphy et al. (2010)
20	952	4.55 ± 0.12	6.98 ± 0.12	0.55 ± 0.01	8.10 ± 0.18	6.98 ± 0.12	9.41 ± 0.27	Murphy et al. (2010)
4.8	39	2.72 ± 0.65	2.35 ± 0.46	1.07 ± 0.43	4.19 ± 1.42	2.35 ± 0.42	7.49 ± 5.61	Sajina et al. (2011)
8.6	39	1.94 ± 0.14	3.39 ± 0.31	1.04 ± 0.10	5.90 ± 1.10	3.41 ± 0.32	10.23 ± 2.95	Sajina et al. (2011)
22	38	2.51 ± 0.10	5.76 ± 0.19	0.82 ± 0.05	8.08 ± 0.44	5.73 ± 0.17	11.40 ± 0.99	Sajina et al. (2011)
43	15	4.74 ± 0.08	9.89 ± 0.20	0.73 ± 0.02	12.43 ± 0.29	9.62 ± 0.13	16.06 ± 0.55	Sajina et al. (2011)

constant during the frequency range studied. To quantify this dependence, we estimate a linear fit on $\langle\Pi^2\rangle^{1/2}$ as a function of a wide (around two orders of magnitude) range of frequencies. This choice is mainly due to the fact that $\langle\Pi^2\rangle$ values are needed to estimate the B-mode angular power spectrum of polarized ERSs and we include in the linear fit also the values of $\langle\Pi^2\rangle^{1/2}$ estimated by Bonavera et al. (2017a) between 30 and 217 GHz. They were derived assuming a log-normal distribution as in this work. In particular, for the best fit, we retain only fractional polarization from the FSRQs and BL Lacs since their contribution dominates number counts at larger fluxes and at frequencies >20 GHz (see Figures 1 and 6). The linear fit involves the data for which the estimation of μ and σ are reliable (filled symbols in Figure 3). Open symbols indicate data that have not been included in the fit, mainly because of the poor statistics in fitting the log-normal distribution (e.g., less than 20 polarized sources have been detected in polarization in the *Planck* HFI channels, see Table 2).

We find a negligible frequency dependence of $\langle\Pi^2\rangle^{1/2}$:

$$\langle\Pi^2\rangle^{1/2}(\nu) = (0.005 \pm 0.006 \text{ GHz}^{-1})\nu$$
$$+ (4.170 \pm 0.22). \tag{6}$$

In the top left panel of Figure 3, we show the linear fit as a gray solid line with darker and lighter shaded areas resembling, respectively, the 1σ and 2σ uncertainties on best-fit parameters. Notice that for $\nu > 20$ GHz, we found $\langle\Pi^2\rangle^{1/2} \sim 4\%$, in agreement with the value found by Tucci & Toffolatti (2012)

and consistent with the expectations of Tucci et al. (2004) and Stil et al. (2014).

At l $\nu < 20$ GHz, SSRQs have to be taken into account to forecast the contribution of ERS to CMB observations. Thus, we perform the same linear fit by including SSRQs for all the data sets at frequencies smaller than 20 GHz, shown in Figure 3 (top right panel). The best-fit equation changes to

$$\langle\Pi^2\rangle^{1/2}(\nu) = (-0.015 \pm 0.009) \text{ GHz}^{-1})\nu$$
$$+ (5.43 \pm 0.23).$$

Nonetheless the slope is still negligible, the presence of SSRQs enhances the average polarization fraction of sources at frequencies $\nu \lesssim 20$ GHz and, as one can notice in Figure 3, this is consistently observed in $\langle\Pi\rangle$ as well.

We would like to stress that selection effects could bias our results toward larger values of Π, especially where few tens of polarized sources have been detected, see Table 2. This is the reason why we excluded PCCS2 HFI data (magenta diamonds) in Figure 3 and we considered the ones from Bonavera et al. (2017a; gray pentagons). To this regard, the stacking technique helps because it includes the faint sources to the statistical estimate of Π even if those sources are not directly detectable.

5. Forecasts for the Forthcoming CMB Ground-based Experiment

In this section, we present the forecast analysis for current and forthcoming CMB surveys performed with a `Python`
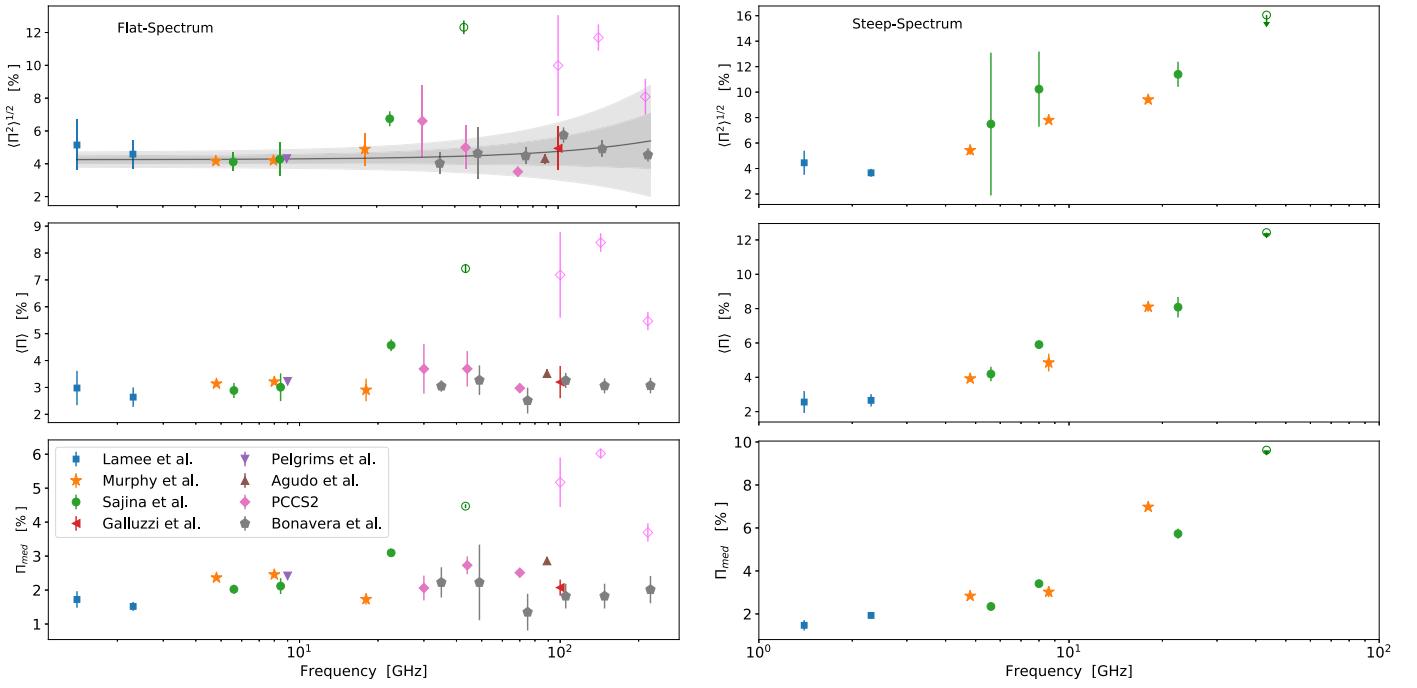
Figure 3. Values of $\langle\Pi^2\rangle^{1/2}$ (top), $\langle\Pi\rangle$ (center), and $\Pi_{\rm med}$ (bottom) derived from best-fit lognormal parameters in (4) and (5). Open symbols are data that have not been taken into account for the linear fit in (6). We distinguished FSRQs (left) from the SSRQs (right). In the top left panel, a linear function is fitted from the data to provide a scaling of polarization fraction as a function of frequency. The light and dark shaded area are the 1σ and 2σ uncertainties, respectively.

Table 3
Nominal Specifics of CMB Experiments Described in Section 5

	Frequency [GHz]	Sensitivity [μK arcmin]	FWHM	$f_{\rm sky}$
QUIJOTE	11, 13, 17, 19	1800	$1°$	50%
CMB-S2	95, 150	25, 30	$3'.5$	5%
CMB-S3 SA	30, 40, 95,150	8, 6, 1, 2	$1°$	20%
CMB-S3 LA	30, 40, 95,150	8, 6, 1, 2	$10', 7', 3', 2'$	20%
LiteBIRD	40, 50, 60, 68, 78	53, 32, 25, 19, 15	$1°$	100%
	89, 100,119, 140,166	12, 15.6, 12.6, 8.3, 8.7	$1°$	100%
CORE150	60, 100, 145	10.6, 7.1, 5.1	$14', 8', 6'$	100%

package Point Source ForeCast (PS4C) made publicly available.[18] PS4C is a user-friendly platform that allows us to forecast the contribution of radio point sources both in total intensity and polarized flux densities given the nominal specifics of a CMB experiment. In Table 3, we summarize the specifics of five CMB experiments with which we forecast the ERS contribution with PS4C:

1. The Q-U-I JOint TEnerife (QUIJOTE López-Caniego et al. 2014) CMB experiment designed to observe the polarized emissions from the CMB, our Galaxy and the extragalactic sources at four frequencies in the range between 10 and 20 GHz and at FWHM resolution of ~1°. Observations started observing in 2012 November, covering 18,000 deg^2 of the northern hemisphere, and achieved the sensitivity of 1800 μK arcmin in polarization.

2. A generic CMB-S2 experiment observing at 95, 150 GHz within a patch including 2% of the sky at the resolution of 3.5 arcmin, at 25 ÷ 30 μK arcmin sensitivity.

3. A CMB-S3 ground-based experiment with the so-called strawman configuration, as it has been defined in

Abazajian et al. (2016), for the "measuring-r" survey. It consists of an array of small-aperture (SA, ~1 m) telescopes and one large-aperture (LA, ~5 m) telescope, observing at the accessible atmospheric windows in the sub-millimeter range (at about 30, 40, 90, and 150 GHz). The sensitivities at these frequencies are targeted to be about 1 ÷ 10 μK arcmin.

4. The Lite satellite for the studies of B-mode polarization and Inflation from cosmic Background Radiation Detection (LiteBIRD Matsumura et al. 2016) is a satellite mission proposed to JAXA aimed at measuring the CMB polarized signal at the degree angular scale. Its goal is to characterize the measurement of r with an uncertainty $\sigma(r) < 0.001$. In order to achieve such high accuracy, the target detector sensitivity is 2 μK arcmin observing over a wide range of frequencies (from 40 to 320 GHz). The current effort aims to launch in 2025.

5. The Cosmic ORigin Explorer (Delabrouille et al. 2017, CORE) is a next-generation space-borne experiment and it has been proposed as a Medium-size ESA mission opportunity. It has been designed as the *Planck* satellite successor, planned to have better angular resolution and sensitivity than *Planck*. We consider the *CORE150* configuration: a satellite involving a 1.5 m telescope,

---

[18] https://gitlab.com/giuse.puglisi/PS4C

observing over a wide range of frequency channels (up to 800 GHz) with sensitivities ranging from ∼10 to 5 μK arcmin. In this work, we restrict our analysis to a selection of frequency channels (see the last row of Table 3) to compare the expectations with the ones previously obtained by De Zotti et al. (2016).

Although most of the frequency channels of future experiments range up to 350 GHz, we forecast up to 150 GHz. This is because, at higher frequencies, the contribution coming from dusty galaxies and Cosmic Infrared Background cannot be neglected[19] (Negrello et al. 2013; De Zotti et al. 2016). Bonavera et al. (2017b) estimated the polarized contribution of dusty galaxies by stacking about 4700 sources observed by *Planck* at 143, 217, and 353 GHz HFI channels. They estimated the polarized contribution of dusty galaxies to B-mode power spectra and found that, at frequencies larger than 217 GHz, this population of sources might remarkably contaminate the primordial B-modes.

We compute one realization of CMB power spectra by means of the CAMB package (Lewis et al. 2000) by assuming the *Planck* best-fit cosmological parameters (Planck Collaboration et al. 2016d) and a tensor-to-scalar ratio $r = 0.05$ (slightly below the current upper limits).

To assess the contribution of ERS to the power spectrum level, we assume their distribution in the sky to be Poissonian, since the contribution of clustering starts to be relevant for $S < 10$ mJy (González-Nuevo et al. 2005; Toffolatti et al. 2005). The power spectrum of temperature fluctuations coming from a Poissonian distribution of sources is expected to be a constant contribution at all multipoles. In particular, we consider as masked all sources whose flux density is above 3σ the detection limit $S_{\text{cut}} = 3\sigma_{\text{det}}$ and we do not include them in the power spectrum estimate

$$C_\ell^T = \left(\frac{dB}{dT}\right)^{-2} N \langle S^2 \rangle = \left(\frac{dB}{dT}\right)^{-2} \int_0^{S_{\text{cut}}} n(S) S^2 dS, \qquad (7)$$

where $n(S)$ and N are, respectively, the differential and the integral number counts per steradian, and dB/dT is the conversion factor from brightness to temperature, being

$$\left(\frac{dB}{dT}\right)^{-1} \approx 10^{-2} \frac{(e^x - 1)^2}{x^4 e^x} \frac{\mu K}{Jy \quad sr^{-1}},$$

with $x = \nu/$ 57 GHz. Tucci et al. (2004) found that it possible to relate the ERS polarization power spectrum to the intensity spectrum (7) as follows

$$C_\ell^Q = \left(\frac{dB}{dT}\right)^{-2} N \langle Q^2 \rangle$$

$$= \left(\frac{dB}{dT}\right)^{-2} N \langle S^2 \Pi^2 \cos^2 2\phi \rangle$$

$$= \left(\frac{dB}{dT}\right)^{-2} N \langle S^2 \rangle \langle \Pi^2 \rangle \langle \cos^2 2\phi \rangle$$

$$= \frac{1}{2}\left(\frac{dB}{dT}\right)^{-2} \langle \Pi^2 \rangle C_\ell^T, \qquad (8)$$

---

[19] We have already planned to include in the package the contribution from dusty galaxies and forecasts with PS4C will be presented in a future release that will be described in a future paper.

where the 1/2 factor comes from the average value of $\cos^2 2\phi$ if the polarization angle ϕ is uniformly distributed. The value for $\langle \Pi^2 \rangle$ is derived at each frequency from Equation (6). Since we do expect point sources to equally contribute on average both to Q and U, and thus to the E and B modes, we can approximate $C_\ell^B \simeq C_\ell^E \simeq C_\ell^U \simeq C_\ell^Q$. In the following, B-mode power spectra are normalized by the usual normalization factor $\mathcal{D}_\ell = \ell(\ell+1) C_\ell / 2\pi$.

To forecast the number of sources that will be detected in intensity and polarized flux density above a given detection limit, we integrate the differential number counts, $n(S)$ and $n(P)$ as

$$N(>S) = \int_{S_{\text{cut}}}^{\infty} n(S) dS, \qquad (9)$$

$$N(>P) = \int_{P_{\text{cut}}}^{\infty} n(P) dP. \qquad (10)$$

Finally, to compare the level of contamination produced by the ERS with the Galactic foreground one, we rescale the Galactic foreground emission at a given f_{sky}, frequency ν and multipole order ℓ as in Planck Collaboration et al. (2016b),

$$\mathcal{D}^{\text{FG}}(\ell, \nu, f_{\text{sky}}) = \frac{\text{Var}[\text{Sync}, f_{\text{sky}}]}{\text{Var}[\text{Sync}, f_{\text{sky},0}]} q_s \left(\frac{\ell}{80}\right)^{\alpha_s} \frac{s_s(\nu)}{s_s(\nu_s)}$$

$$+ \frac{\text{Var}[\text{Dust}, f_{\text{sky}}]}{\text{Var}[\text{Dust}, f_{\text{sky},0}]} q_d \left(\frac{\ell}{80}\right)^{\alpha_d} \frac{s_d(\nu)}{s_d(\nu_d)}, \qquad (11)$$

with s and d referring, respectively, to synchrotron and dust. For all the parameters entering in (11), we use the best-fit values quoted in Table 11 of Planck Collaboration et al. (2016b) estimated outside the Galactic plane in the UPB77 mask (Planck Collaboration et al. 2016a, defined in Section 4.2). The mask has been computed considering a common foreground mask after component separation analysis with the 1° apodization scale. Therefore, to rescale the estimate in Equation (11) to a patch with a smaller fraction of sky, f_{sky}, we need to compute the variance of both synchrotron and thermal dust template maps within the considered patch and within the *Planck* region with $f_{\text{sky},0} = 73\%$. The rescaled foreground power spectra are shown in Figure 4 as dotted lines.

5.1. PS4C with Current and Forthcoming CMB Ground-based Experiments

Figure 4 shows our PS4C forecasts of foreground contamination to the recovery of the CMB B-mode for the different experiments in the different panels: we plot the expected spectrum in polarization of Galactic (dotted lines) and ERS (dashed lines) emissions at the different frequencies available for each experiment and the total CMB B-mode power spectrum (black solid line). The black dotted–dashed lines show the primordial ($r = 0.05$) and lensed B-mode power spectra separately. The power spectra are computed in the region outside the UPB77 *Planck* mask (in order to exclude the Galactic plane and the ERS whose flux density is below the 3σ detection limit). The Galactic foreground turns out to be the most contaminating emission in the B-mode recovery. The different colors for the Galactic and ERS spectra are for different frequencies, going from purple to yellow as the frequency increases. It should be commented that there exist
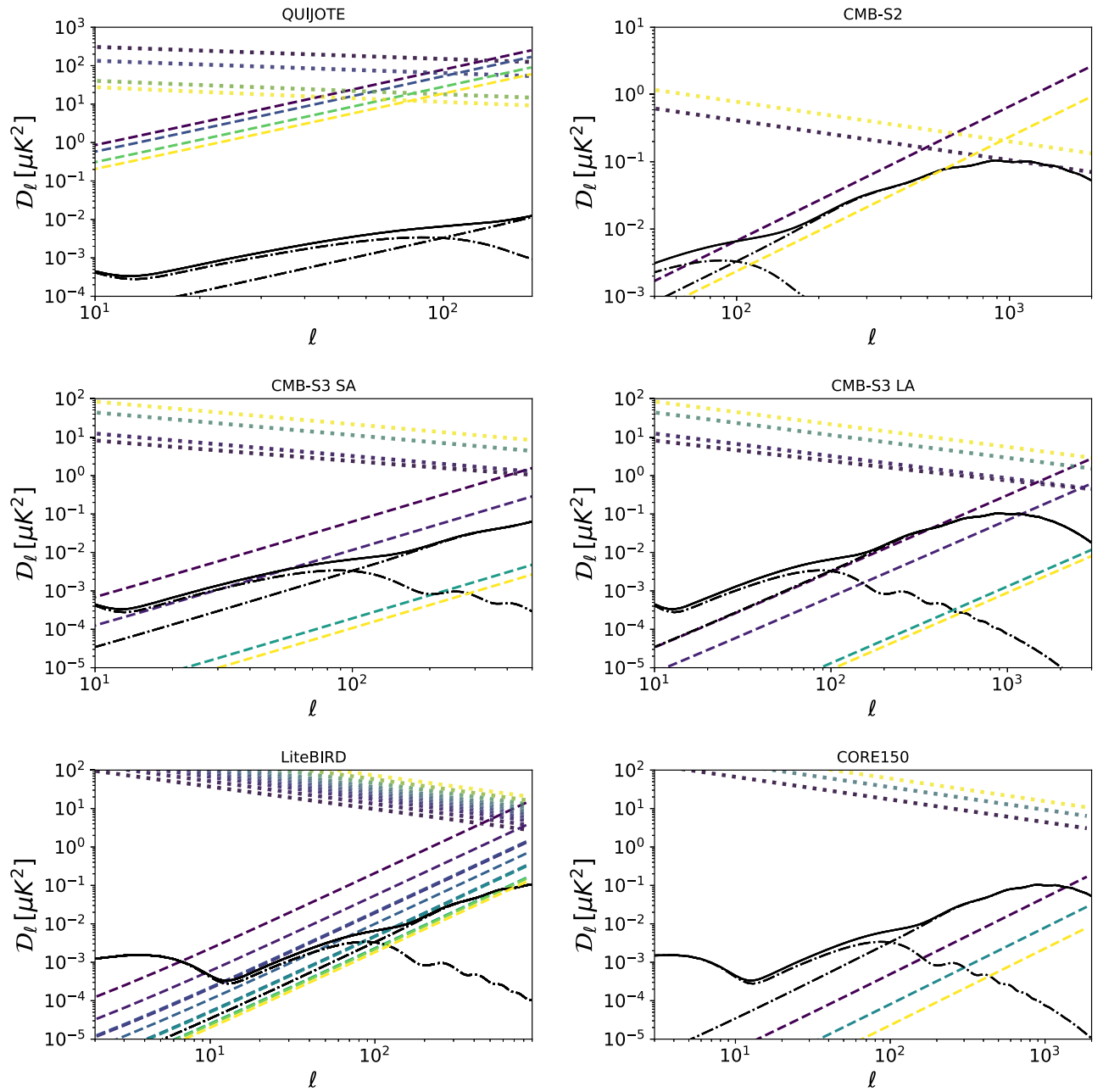
Figure 4. Forecasts of foreground contamination with PS4C. In all panels, the black dotted–dashed lines show the primordial ($r = 0.05$) and lensed CMB B-mode power spectra and the black solid line is the the total CMB B-mode power spectrum. The dotted (dashed) lines are the power spectrum of the polarized Galactic emission (ERS emission) at the different frequencies available for each experiment, the color scale is such that the colors go from purple to yellow as the frequency increases. The power spectra depend are estimated using Equation (11) in the region outside the UPB77 *Planck* mask (in order to exclude the Galactic plane and ERS above the 3σ detection limit). The different panels corresponds to predictions for different experiments. From top to bottom and from left to right: QUIJOTE (11, 13, 17, and 19 GHz), CMB-S2 (95 and 150 GHz), CMB-S3 observing with small- and large-aperture telescopes (30, 40, 95, and 150 GHz), LiteBIRD (frequencies between 40–166 GHz), and CORE150 (60, 100, and 145 GHz).

several component separation and foreground cleaning algorithms that can recover CMB intensity and polarization signals with great accuracy (Planck Collaboration et al. 2016b). In addition, multi-frequency observations and joint analyses from different experiments (BICEP2/Keck & Planck Collaborations et al. 2015) can improve the foreground cleaning. So, even if in our work we are considering the most conservative cases, it should be stressed that such contamination could be lowered (at the sub-percentage level; Errard et al. 2011; Stompor et al. 2016) by applying such foreground removal algorithms.

In particular, Figure 4 shows our forecasts for the QUIJOTE (top left) and CMB-S2 (top right) experiments. As for QUIJOTE, the Galactic emission is much higher than the CMB emission and higher than the contribution from undetected ERS, except at small angular scales where the ERS start to be dominant. Since the QUIJOTE experiment ranges from 10 to 20 GHz, we need to take into account the contribution from both FSRQs and SSRQs, with the resulting increase in the average fractional polarization and number counts (see Figure 3 and Figure 6). Table 4 summarizes the total number of sources in
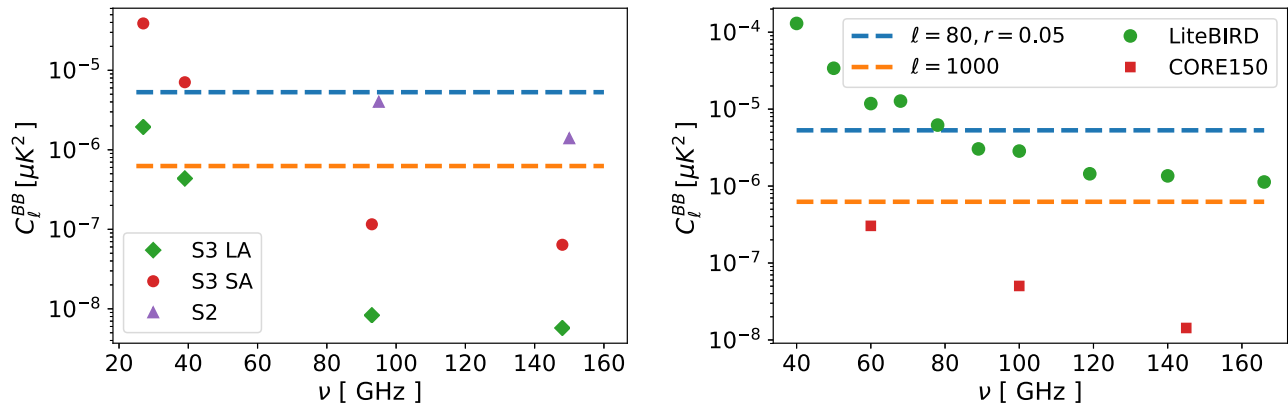
Figure 5. Power spectra in polarization of undetected ERS in current and future CMB experiments. Left panel: CMB-S2 (triangles) and CMB-S3 (circles for the small-aperture telescope and diamonds for the large-aperture telescope). Right panel: LiteBIRD (circles) and CORE150 (squares). The dotted lines are the B-mode power spectra at the acoustic scale ($\ell = 80$) and at the lensing B-modes peak scale ($\ell \approx 1000$).

total intensity (third column) and polarization (fourth column) that QUIJOTE would detect (frequencies are given in the first column), assuming nominal and conservative sensitivity values (flux density limits in total intensity and polarization are listed in columns two and three, respectively). We found 694, 445, 201, and 128 sources in total intensity at 11, 13, 17, and 19 GHz, respectively. In polarization, only a few of them would be detected and just in the 11 and 13 GHz channels.

For the CMB-S2 experiment whose frequencies are greater than 95 GHz, the Galactic emission (mostly thermal dust emission) is the most contaminating up to $\ell \sim 350$, while the ERS are important at small angular scales. Unlike the previous case, at these frequencies the CMB B-mode spectrum is comparable to that of undetected ERS.

In Figure 5, the triangles show the C_ℓ^{BB} of undetected ERS estimated using Equation (8). The detection limits are given by the CMB-S2 sensitivities. The C_ℓ^{BB} of the CMB B-mode are also plotted: the cyan dashed line is for the case $\ell \approx 80$ and $r = 0.05$ and the orange dashed line is for $\ell \approx 1000$. Figure 5 shows what is the contamination due to undetected ERS and consequently the level of source detection required to detect the primordial or lensing B-mode signal. In CMB-S2, the undetected ERS level of the power spectrum is comparable to the lensing B-mode level. In this case, given the experiment sensitivity and the size of the observed region, ~150 sources would be detected in total intensity and only a few of them in polarization at a 3σ level.

Among the experiments studied in this work, the CMB-S3 is the one with the greatest sensitivity and best resolution. The results are shown in the central panels of Figure 4 and in the left panel of Figure 5 with circles and diamonds. As summarized in Table 5, the maximum number of polarized sources detected above a 3σ level and using the large-aperture telescope is 2329 with flux density $P_{\rm lim} \gtrsim 1$ mJy. When using a smaller aperture telescope, this number drops to a few hundred with polarized flux densities $P_{\rm lim} \gtrsim 10$ mJy.

The contribution in polarization of undetected ERS is very small at high frequencies ($\nu \gtrsim 90$) and at low multipoles $\ell \lesssim 2000$. At lower frequencies, undetected ERS still can contaminate and they have to be taken into account to de-lens, lensing B-modes to get the primordial ones for $r \lesssim 0.05$.

5.2. PS4C with Future Space Missions

The results for the LiteBIRD experiment are shown in the left bottom panel of Figure 4 and the filled circles in the right panel of Figure 5. On the whole, the most contaminating contribution is the Galactic one, except at small angular scales ($l \sim 400$) and high frequencies ($\nu > 70$ GHz) where the ERS contribution is comparable to the Galactic one. The ERS contribution, although generally lower than the Galactic one, is also important, being higher than the CMB B-mode level even at large scales ($l \gtrsim 7$) and $\nu < 70$ GHz (dashed purple and blue lines). Moreover, at $\nu > 80$ GHz and $l \gtrsim 70$, the ERS contribution is comparable to the B-mode power spectrum. The number of sources that would be detected in polarization above the 3σ level with this experiment are listed in Table 6 and they range from 4 at 10 and 68 GHz to 14 at 119 GHz. The first column is the frequency in gigahertz, the second is the polarized flux density limit in millijansky, and the third column is the number of sources that would be detected by LiteBIRD (values in the brackets are estimated from the C2Ex model).

Our findings for CORE are shown in the right bottom panel of Figure 4 and in the right panel of Figure 5 (squares). Galactic emission is the most contaminating for B-mode detection. Undetected ERS are important only at 60 GHz, where their power spectrum is comparable to that of the B-mode due to lensing. CORE would be able to detect up to 200 sources per steradian, implying a lower contamination for the CMB B-mode power spectrum with respect to LiteBIRD.

Table 7 compares the surface densities (i.e., number of sources per steradian, last two columns) at CORE frequencies (first column) of the polarized ERS above the $P_{4\sigma}$ flux density limit (second column) estimated by De Zotti et al. (2016) (DZ16) and PS4C (values in the brackets are for C3Ex estimate). In this comparison, we use a 4σ flux density limit in order to be consistent with the estimates by De Zotti et al. (2016). Above 100 GHz, we find a discrepancy between D05 and DZ16 that could be due to two effects that become more important at higher frequencies: (i) the D05 predictions tend to overestimate the polarized source number counts (see Section 3) and (ii) at $\nu > 100$ the polarization fraction is expected to suffer a slight increase (from ~4% to ~5% from 100 to 150 GHz) as can be seen in Equation (6) and Figure 3.

Table 4
Number of Sources Detected above the $\geqslant S_{lim}$ and $\geqslant P_{lim}$ Flux Densities Limit by the QUIJOTE Experiment, Assuming the Nominal and Conservative Values for Sensitivity

ν[GHz]	S_{lim} [Jy]	N_{src}	P_{lim} [Jy]	N_{src}
11	0.5	694 (673)	0.5	6 (4)
	1	347 (340)	1	2 (1)
13	0.5	445 (434)	0.5	2 (1)
	1	210 (205)	1	0 (0)
17	1	201 (197)	1	0 (0)
	2	86 (83)	2	0 (0)
19	1	128 (125)	1	0 (0)
	2	52 (51)	2	0 (0)

Note. Values are estimated using D05 and C2Ex models (ins brackets).

Table 5
Number of Polarized ERS Detected above the $P_{3\sigma}$ Flux Density Detection Limit in Polarization, by Current and Forthcoming CMB Ground-based Experiments

	CMB -S2		CMB -S3			
			SA		LA	
	$P_{3\sigma}$		$P_{3\sigma}$		$P_{3\sigma}$	
ν[GHz]	[mJy]	$N_{3\sigma}$	[mJy]	$N_{3\sigma}$	[mJy]	$N_{3\sigma}$
30	...	...	15	236 (191)	1.5	2329 (2278)
40	...	...	15	215 (156)	1.5	1867 (1810)
95	100	3 (2)	10	355 (222)	1	2432 (2136)
150	100	3 (1)	15	146 (74)	1.5	1145 (867)

Note. Counts are estimated both from the D05 and the C2Ex predictions (in brackets).

Table 6
Number of Sources Observed above the $3\sigma_{det}$ Limit in Terms of Polarized Flux Density $P_{3\sigma}$ by the LiteBIRD Experiment

ν [GHz]	$P_{3\sigma}$ [mJy]	$N_{3\sigma}$
40	450	4 (3)
50	240	11 (8)
60	210	9 (6)
68	300	4 (3)
78	240	6 (4)
89	210	12 (8)
100	240	10 (7)
119	210	14 (10)
140	270	8 (4)
166	270	7 (4)

Note. Bracketed values are estimated using the C2Ex model.

Table 7
Comparison of Surface Densities of Polarized ERSs Brighter than $P_{4\sigma}$ Estimated by De Zotti et al. (2016) (DZ16) and by PS4C

ν [GHz]	$P_{4\sigma}$ [mJy]	$N_{4\sigma}$ [sr^{-1}]	
		DZ16	PS4C
60	5.2	212	214 (198)
100	5.2	184	229 (164)
145	4.6	165	271 (142)

Note. Values in brackets refer to C2Ex estimates.

On one hand, at 100 GHz, we find that accounting solely for the observation in (ii), i.e., a 20% increase of Π to a value of 4.67%, the D05 forecasts predict source counts that are 20% larger than DZ16.[20] On the other hand, at 150 GHz, the surface density estimated with PS4C with D05 model is ∼65% larger than the value referred by DZ16. Even accounting for the 25% fractional increase of Π to 4.92% from Equation (6), this is not enough to compensate for the observed discrepancy. We thus argue that the discrepancy at 150 GHz is caused by both (i) and (ii).

Contrary to the D05 forecasts, the C2Ex model is in reasonable agreement with De Zotti et al. (2016), meaning that the C2Ex predictions are more robust than the D05 predictions at least at higher frequencies.

6. Summary and Conclusions

We describe and present the state-of-the-art observations on polarization of ERS over a wide frequency range, namely from 1.4 to 217 GHz. We exploit for the first time the polarization number counts at 95 GHz from a sample of 32 polarized sources detected with ALMA. The characterization of these sources and their spectral behavior in frequencies ranging from 1 to 95 GHz are described in a companion paper by V. Galluzzi et al. (2018, in preparation)

By collecting polarization flux densities from 10 catalogs, we are able to derive a relation of the average fractional polarization as a function of frequency and to avoid extrapolations that have been commonly adopted to forecast the average polarization fraction from low- ($\lesssim$20 GHz, where enough data have been collected), to high-frequency ($\gtrsim$70 GHz, where few polarization measurements have been performed). Therefore, we fit a linear function on data from several surveys, including *Planck* measurements from both detection and stacking, and we find a mild dependence of $\langle \Pi^2 \rangle^{1/2}$ as a function of ν.

This relation allows us to forecast the contribution of ERSs to the polarization B-mode power spectrum given the nominal sensitivities of current and forthcoming CMB experiments, by means of predictions of ERS counts coming from two models, D05 and C2Ex. The whole forecast suite is fully integrated into a `Python` package, PS4C, made publicly available with online documentation and tutorials.

We discuss the reasons why we do not assume a correlation between the level of fractional polarization and the total intensity flux. Although still controversial and not observed at high radio frequencies (Massardi et al. 2013; Galluzzi et al. 2017, 2018, V. Galluzzi et al. 2018, in preparation), deeper surveys in polarization are critical to provide further proof of the validity of this assumption, not only at higher frequencies but also at fainter flux density levels.

Future CMB experiments could shed light on this interesting aspect: in fact, we have shown that they are going to observe an increasing number of polarized ERS (they are foreseen to detect up to ∼2000 polarized ERS) because their sensitivity will increasingly improve in the future.

A further potentiality of future CMB experiments is that they can be largely exploited by the community as wide global

---

[20] For this estimate, we assume that differential source counts are described by a power law with spectral index >1.

surveys to measure the polarized flux density of sources at very high radio frequencies (Partridge et al. 2017). Programs aimed at observing ERSs at higher resolution can thus benefit of CMB large area surveys in an extremely wide range of frequencies, from 20 up to 300 GHz.

Moreover, since in this work we mostly focus on blazar statistical polarization, as it is the main bright source population at frequencies <150 GHz, we restrict our forecast analysis up to this frequency limit. At higher frequencies, the far-IR dusty star-forming galaxies constitute the majority of extragalactic sources (see Figure 25 Planck Collaboration 2015) and, similarly to the ERSs, their polarized emission contaminates B-mode power spectra[21] (De Zotti et al. 2015). Recent works from Bonavera et al. (2017b) and De Zotti et al. (2016) have already shown statistical polarization properties of dusty sources and forecasted their contribution for future CMB experiments. Therefore, we plan to include those estimates within the PS4C package in a future development.

As a final remark, we stress that ERSs below the detection flux limit may introduce a bias at all the angular scales and at frequencies $\nu < 50$ GHz: their synchrotron emission is still strong enough to contaminate polarization measurements even at low flux densities, namely $P < 1$ mJy. At larger frequencies, ERS polarization power spectra have to be assessed as long as smaller angular scales are involved to estimate the CMB power spectrum at multipoles around the lensing peak or to estimate the primordial B-mode power spectrum at lower multipoles ($\ell < 800$) by means of de-lensing algorithms.

Appendix

We show in Figure 6 a comparison of the predictions from D05 (solid black) and C2Ex (solid grey) models on a wide range of frequencies. Flux-density differential number counts from different surveys are shown as data points (see references in the caption of Figure 6). As discussed in Section 3, predictions from the two models are fairly consistent at frequencies below 70 GHz, whereas at higher values the D05 model tends to over-predict the observed source counts.
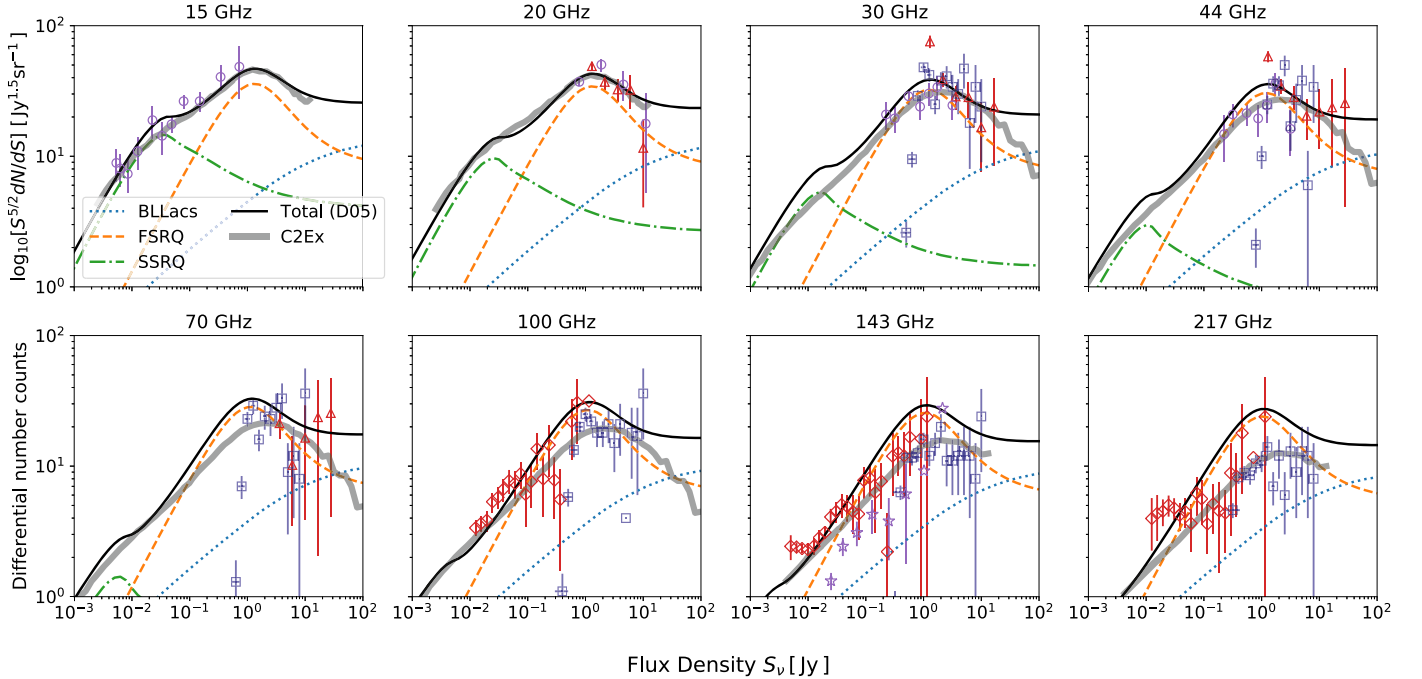

Figure 6. Euclidean normalized differential number counts on a wide range of frequencies. The dotted, dashed, dotted–dashed and solid lines are respectively the number counts of BL Lacs, FSRQs, SSRQs and their total contribution predicted by the D05 model. The thick solid gray line are the number counts coming from the C2Ex model. Number counts obtained with several experiments observing at similar frequency channels are also shown: open circles at 15 and 20 GHz are, respectively, from Waldram et al. (2003, 2010) and Massardi et al. (2008); open circles at 30 and 44 GHz resemble counts from the PACO data set (Bonavera et al. 2011); upper triangles from 20 to 70 GHz are data from WMAP5-yr survey (Massardi et al. 2009); diamonds at 100, 143, and 217 GHz are from SPT (Mocanu et al. 2013); stars at 143 GHz are ACT counts (Marriage et al. 2011); squares at 30, 44, 70, 100, 143, and 217 GHz are based on data from Planck Collaboration et al. (2011b).

---

[21] In addition to the Poissonian contribution, an extra-term coming from clustering has to be considered when dusty sources are involved.

[22] http://www.cosmosnet.it

ORCID iDs

G. Puglisi ⓘ https://orcid.org/0000-0002-0689-4290
J. Gonzalez-Nuevo ⓘ https://orcid.org/0000-0003-1354-6822
A. Lapi ⓘ https://orcid.org/0000-0002-4882-1735
A. Celotti ⓘ https://orcid.org/0000-0002-8106-2777

References

Abazajian, K. N., Adshead, P., Ahmed, Z., et al. 2016, arXiv:1610.02743
Agudo, I., Thum, C., Wiesemeyer, H., & Krichbaum, T. P. 2010, ApJS, 189, 1
Arnold, K., Stebor, N., Ade, P. A. R., et al. 2014, Proc. SPIE, 9153, 91531F
Austermann, J. E., Aretxaga, I., Hughes, D. H., et al. 2009, MNRAS, 393, 1573
Battye, R. A., Browne, I. W. A., Peel, M. W., Jackson, N. J., & Dickinson, C. 2011, MNRAS, 413, 132
Benson, B. A., Ade, P. A. R., Ahmed, Z., et al. 2014, Proc. SPIE, 9153, 91531P
BICEP2/Keck & Planck Collaborations, Ade, P. A. R., Aghanim, N., et al. 2015, PhRvL, 114, 101301
Blandford, R. D., & Koenigl, A. 1979, ApL, 20, 15
Bonaldi, A., Bonavera, L., Massardi, M., & De Zotti, G. 2013, MNRAS, 428, 1845
Bonato, M., Negrello, M., Mancuso, C., et al. 2017, MNRAS, 469, 1912
Bonavera, L., González-Nuevo, J., Argüeso, F., & Toffolatti, L. 2017a, MNRAS, 469, 2401
Bonavera, L., González-Nuevo, J., De Marco, B., Argüeso, F., & Toffolatti, L. 2017b, MNRAS, 472, 628
Bonavera, L., Massardi, M., Bonaldi, A., et al. 2011, MNRAS, 416, 559
Condon, J. J., Cotton, W. D., Greisen, E. W., et al. 1998, AJ, 8065, 1693
Curto, A., Tucci, M., González-Nuevo, J., et al. 2013, MNRAS, 432, 728
De Zotti, G., Castex, G., González-Nuevo, J., et al. 2015, JCAP, 6, 018
De Zotti, G., Gonzalez-Nuevo, J., Lopez-Caniego, M., et al. 2016, arXiv:1609.07263
De Zotti, G., Massardi, M., Negrello, M., & Wall, J. 2010, A&ARv, 18, 1
de Zotti, G., Ricci, R., Mesa, D., et al. 2005, A&A, 431, 893
Delabrouille, J., de Bernardis, P., Bouchet, F. R., et al. 2017, arXiv:1706.04516
Errard, J., Stivoli, F., & Stompor, R. 2011, PhRvD, 84, 069907
Galluzzi, V., & Massardi, M. 2016, IJMPD, 25, 1640005
Galluzzi, V., Massardi, M., Bonaldi, A., et al. 2017, MNRAS, 465, 4085
Galluzzi, V., Massardi, M., Bonaldi, A., et al. 2018, MNRAS, 475, 1306
Gehrels, N. 1986, ApJ, 303, 336
Goldreich, P., & Kylafis, N. D. 1981, ApJL, 243, L75
González-Nuevo, J., Toffolatti, L., & Argüeso, F. 2005, ApJ, 621, 1
Guth, A. H. 1981, PhRvD, 23, 347
Henderson, S. W., Allison, R., Austermann, J., et al. 2016, JLTP, 184, 772
Hu, W., & White, M. J. 1997, NewA, 2, 323
Jackson, N., Battye, R. A., Browne, I. W. A., et al. 2007, MNRAS, 376, 371
Jackson, N., Browne, I. W. A., Battye, R. A., Gabuzda, D., & Taylor, A. C. 2010, MNRAS, 401, 1388
Keisler, R., Hoover, S., Harrington, N., et al. 2015, ApJ, 807, 151
Kellermann, K. I. 1966, ApJ, 146, 621
Lamee, M., Rudnick, L., Farnes, J. S., et al. 2016, ApJ, 829, 5
Lewis, A., Challinor, A., & Lasenby, A. 2000, Astrophys.J., 538, 473
Lopez-Caniego, M., Massardi, M., Gonzalez-Nuevo, J., et al. 2009, ApJ, 705, 868

López-Caniego, M., Rebolo, R., Aguiar, M., et al. 2014, arXiv:1401.4690
Louis, T., Grace, E., Hasselfield, M., et al. 2017, JCAP, 6, 031
Mancuso, C., Lapi, A., Prandoni, I., et al. 2017, ApJ, 842, 95
Marriage, T. A., Baptiste Juin, J., Lin, Y.-T., et al. 2011, ApJ, 731, 100
Massardi, M., Bonaldi, A., Bonavera, L., et al. 2011, MNRAS, 415, 1597
Massardi, M., Burke-Spolaor, S. G., Murphy, T., et al. 2013, MNRAS, 436, 2915
Massardi, M., Ekers, R. D., Murphy, T., et al. 2008, MNRAS, 384, 775
Massardi, M., Ekers, R. D., Murphy, T., et al. 2011, MNRAS, 412, 318
Massardi, M., López-Caniego, M., González-Nuevo, J., et al. 2009, MNRAS, 392, 733
Matsumura, T., Akiba, Y., Arnold, K., et al. 2016, JLTP, 184, 824
Mocanu, L. M., Crawford, T. M., Vieira, J. D., et al. 2013, ApJ, 779, 61
Murphy, T., Sadler, E. M., Ekers, R. D., et al. 2010, MNRAS, 402, 2403
Negrello, M., Clemens, M., Gonzalez-Nuevo, J., et al. 2013, MNRAS, 429, 1309
Partridge, B., Bonavera, L., López-Caniego, M., et al. 2017, Galax, 5, 47
Pelgrims, V., & Hutsemékers, D. 2015, MNRAS, 450, 4161
Planck Collaboration 2015, A&A, 594, A26
Planck Collaboration, Aatrokoski, J., Ade, P. A. R., et al. 2011a, A&A, 536, A15
Planck Collaboration, Adam, R., Ade, P. A. R., et al. 2016a, A&A, 594, A9
Planck Collaboration, Adam, R., Ade, P. A. R., et al. 2016b, A&A, 594, A10
Planck Collaboration, Adam, R., Ade, P. A. R., et al. 2016c, A&A, 586, A133
Planck Collaboration, Ade, P. A. R., Aghanim, N., et al. 2011b, A&A, 536, A13
Planck Collaboration, Ade, P. A. R., Aghanim, N., et al. 2013, A&A, 550, A133
Planck Collaboration, Ade, P. A. R., Aghanim, N., et al. 2016d, A&A, 594, A13
Planck Collaboration, Ade, P. A. R., Aghanim, N., et al. 2016e, A&A, 594, A25
Puglisi, G., Fabbian, G., & Baccigalupi, C. 2017, MNRAS, 469, 2982
Sajina, A., Partridge, B., Evans, T., et al. 2011, ApJ, 732, 45
Seljak, U., & Zaldarriaga, M. 1997, PhRvL, 78, 2054
Starobinsky, A. A. 1982, PhLB, 117, 175
Stil, J. M., Keller, B. W., George, S. J., & Taylor, A. R. 2014, ApJ, 787, 99
Stompor, R., Errard, J., & Poletti, D. 2016, PhRvD, 94, 083526
The Polarbear Collaboration, Ade, P. A. R., Aguilar, M., et al. 2017, ApJ, 848, 121
The Polarbear Collaboration, Ade, P. A. R., Akiba, Y., Anthony, A. E., et al. 2014, ApJ, 794, 171
Toffolatti, L., Negrello, M., González-Nuevo, J., et al. 2005, A&A, 438, 475
Trombetti, T., Burigana, C., De Zotti, G., Galluzzi, V., & Massardi, M. 2017, arXiv:1712.08412
Tucci, M., Martínez-González, E., Toffolatti, L., González-Nuevo, J., & De Zotti, G. 2004, MNRAS, 349, 1267
Tucci, M., & Toffolatti, L. 2012, AdAst, 2012, 52
Tucci, M., Toffolatti, L., De Zotti, G., & Martínez-González, E. 2011, A&A, 533, A57
Vieira, J. D., Crawford, T. M., Switzer, E. R., et al. 2010, ApJ, 719, 763
Waldram, E. M., Pooley, G. G., Davies, M. L., Grainge, K. J. B., & Scott, P. F. 2010, MNRAS, 404, 1005
Waldram, E. M., Pooley, G. G., Grainge, K. J. B., et al. 2003, MNRAS, 342, 915
Wright, E. L., Chen, X., Odegard, N., et al. 2009, ApJS, 180, 283